IOP Publishing Classical and Quantum Gravity
Class. Quantum Grav. **37** (2020) 075015 (13pp) https://doi.org/10.1088/1361-6382/ab7716

Designing arm cavities free of parametric instability for gravitational wave detectors

Jue Zhang[1], **Chunnong Zhao, Li Ju and David Blair**

Department of Physics, The University of Western Australia, Australia

E-mail: zhangjue.astro@gmail.com

Received 21 October 2019, revised 14 February 2020
Accepted for publication 17 February 2020
Published 5 March 2020

Abstract

Parametric instability is an intrinsic problem in high power laser interferometer gravitational wave detectors. Optical cavity modes interact with acoustic modes of the test masses, leading to laser power dependent exponential growth of acoustic vibration of the test masses. Future detectors are being planned with designed optical power as high as 5 MW. This increases the requirements for suppressing of parametric instability through various currently available methods. Parametric instabilities could also be alleviated through careful design of the acoustic mode structure and optical mode spacing. Here we study parametric instabilities in future gravitational wave detectors with arm lengths between 6 and 10 km. We show that by careful choice of test mass radii of curvature, dimensions and arm lengths it is possible to design detectors that are free of parametric instability up to 3 MW of intra-cavity power with large enough tolerance on mirror radii of curvature change. We present several case studies and give an example of a design with 6335 m arm cavities and test mass diameter of 52 cm that is parametric instability free. This design is relatively tolerant, staying free of instabilities for a 45 m change in test mass radius of curvature. Maintaining this radius of curvature could easily be done with good design and thermal compensation.

Keywords: gravitational wave, parametric instability, PI-free window

1. Introduction

The network of Advanced LIGO [1] and Advanced Virgo [2] has successfully detected binary black hole coalescence [3], binary neutron star coalescences [4]. A full list of candidate events can be found in [5, 6]. The direct detections of gravitational waves (GW) have motivated the desire to construct more gravitational wave detectors with higher sensitivity. KAGRA [7] and LIGO-India [8] will join the network in the near future and should provide better network duty

[1] Author to whom any correspondence should be addressed.

cycle and event localization. The proposed future detectors include the 10 km Einstein telescope [9], 40 km Cosmic Explorer [10], an Asia/Australia 8 km detector [11] and the OzGrav high frequency detector [12]. Future detectors are expected to operate with very high intra-cavity power up to several MW to lower the shot noise and achieve better sensitivity. These conditions will excite parametric instability (PI) which occurs when cavity laser power excites the acoustic modes of test masses, leading to exponential growth of acoustic modes and eventual loss of control of the cavity. PI was theoretically predicted by Braginsky [13] and observed in suspended cavities, table top experiment, and Advanced LIGO [14–16]. The success of the first three observing runs of Advanced LIGO and Advanced VIRGO has in part been due to the PI mitigation strategies including thermal detuning [17] where thermal gradients across the test mass induce changes in radius of curvature (RoC) to detune optical mode frequencies from acoustic modes; active damping [18] with electrostatic actuation on the test mass, and passive damping [19] by attaching acoustic mode dampers to lower the Q factor. Optical feedback is another method of instability suppression, involving injection of a higher order mode to cancel the internally generated higher order mode, effectively lowering the optical mode Q factor. This technique is still being studied [20, 21].

All proposed future detectors share some features in common: larger test masses, longer arm lengths, and higher intra-cavity power. PI in future detectors remains a potential problem because the mode density increases in larger test masses and parametric gain is proportional to the intra-cavity power. For example, simulations of PI in LIGO Voyager [22] based on single cavity case [23] with silicon test masses, indicates there will be comparable PI problems as those in LIGO today.

In this paper, we analyze PI in possible future gravitational wave detectors using a single cavity model. Previous studies have shown that dual recycling cavities have a significant effect on parametric instability, particularly maximum parametric gain and the radius of curvature of the test mass mirrors that produce maximum parametric gain [24–26]. However this results from splitting of the resonance of arm cavity with the additional recycling cavities and is therefore reliant on there being some arm cavity resonance. Therefore the modeling of an arm cavity presented in this paper provides a useful preliminary analysis, indicative of PI-free designs. This method may be extended in the future design processes to provide minimal PI in the next generation of gravitational wave detectors.

Our aim is to investigate whether it is possible to choose interferometer parameters that could be free of PI. In practice, not all parameters can be perfectly predicted in the design process and parameters such as mirror RoC which varies with thermal distortion from absorbed laser power and ring heater compensation. Here we focus on finding a detector parameter space free from PI. Particularly we look for ranges of RoC within which all acoustic modes have parametric gain below unity—we call this a *PI-free window*. In section 2, we introduce the theory and simulate PI in an 8 km arm cavity. In section 4, we analyze PI-free windows for test masses with different diameters in a single cavity with 6–10 km arm length. The purpose is to discover an optimal design which includes the biggest PI-free window.

2. Parametric instability

Parametric instability severity in the single cavity configuration is described by the parametric gain R as shown in equation (1) [27]. Any acoustic mode with R above unity is unstable.

$$R = R_{\mathrm{s}} - R_{\mathrm{a}} = \frac{4PQ_{\mathrm{m}}}{McL\omega_{\mathrm{m}}^2}\left(\sum_k\sum_m\sum_n \frac{\Lambda Q_{\mathrm{s}}}{1+\left(\frac{\triangle\omega_{\mathrm{s}}}{\delta_{\mathrm{s}}}\right)^2} - \sum_k\sum_m\sum_n \frac{\Lambda Q_{\mathrm{a}}}{1+\frac{\triangle\omega_{\mathrm{a}}^2}{\delta_{\mathrm{a}}^2}}\right), \tag{1}$$

where P represents the intra-cavity power in the cavity arm, Q_{m} and $Q_{\mathrm{s,a}}$ are the quality factors of the acoustic mode and optical modes, M is the mass of the test mass, L is the length of the cavity, ω_{m} is the frequency of the acoustic mode, summation indices k, m and n indicate the order of higher order longitudinal and transverse modes used in the analysis that describe the full set of possible Stokes and anti-Stokes diagram, Λ is the spatial overlapping factor and δ is the half line-width of the optical mode. Subscripts s and a indicate Stokes and anti-Stokes processes respectively. The frequency detuning parameter is given by

$$\triangle\omega_{\mathrm{s,a}} = |\omega_{\mathrm{kmn}} - \omega_{00}|_{\mathrm{s,a}} - \omega_{\mathrm{m}}, \tag{2}$$

with ω_{00} being the cavity carrier and ω_{kmn} the transverse higher order mode frequency, $|\omega_{\mathrm{kmn}} - \omega_{00}|_{\mathrm{s,a}} = k \cdot \mathrm{fsr} + \frac{(m+n)c}{L} \mathrm{acos}\sqrt{g_1 g_2}$, where k is the longitudinal mode order, $\mathrm{fsr} = \pi c/L$ is the free spectral range, g factor $g_{1,2} = 1 - \frac{L}{\mathrm{RoC}_{1,2}}$, and $0 < g_1 g_2 < 1$ indicates a stable cavity [28]. In the Stokes process ($\omega_{\mathrm{m}} \sim \omega_{00} - \omega_{\mathrm{kmn}}$), optical power is transferred to an acoustic mode, which corresponds to parametric gain $R > 0$. In the anti-Stokes process ($\omega_{\mathrm{m}} \sim \omega_{\mathrm{kmn}} - \omega_{00}$), the acoustic mode transfers energy to the optical mode, the acoustic mode is damped, $R < 0$. Stokes and anti-Stokes processes both occur in optical cavities but seldom cancel out, as optical transverse modes have asymmetric structure around the carrier [13]. The spatial overlapping factor in equation (1) is given as [13]

$$\Lambda = \frac{V(\int E^{00}(\vec{r})E^{\mathrm{mn}*}(\vec{r})\mu_{\perp}(\vec{r})\mathrm{d}\vec{r_{\perp}})^2}{\int |\mu(\vec{r})|^2 \mathrm{d}V \int |E^{00}(\vec{r})|^2 \mathrm{d}\vec{r_{\perp}} \int |E^{\mathrm{mn}}(\vec{r})|^2 \mathrm{d}\vec{r_{\perp}}}, \tag{3}$$

where V represents the volume of the test mass, E^{00} and E^{mn} are the field distributions of the fundamental mode and higher order mode, μ and $\mu_{\perp}$ are the test mass total and surface amplitude displacements of the acoustic mode.

When both (a) the frequency of an acoustic mode matches the frequency difference between the fundamental mode and the higher order mode, and (b) the overlap between acoustic and the beating of optical fundamental and higher order mode is large, the parametric gain R can exceed unity. Once $R > 1$, the beating of the fundamental optical mode and the scattered higher order modes by the thermal motion of the test mass acoustic modes will in turn drive the acoustic mode, which causes the acoustic mode amplitude growing exponentially, leading to the difficulty in interferometer operation. In the following sections parametric gain sensitivity to changes in cavity length, test mass radius of curvature and test mass size is explored to find interferometer designs that are PI-free.

3. Parametric instability in an 8 km cavity

To model the parametric gain we use the analytic expressions of equation (1). The mechanical eigen-frequency ω_{m} and mode shape $\mu_{\perp}(\vec{r})$ are simulated in COMSOL. The Hermite Gaussian basis is assumed for the optical mode shape. Based on the model proposed in Asia/Australia 8 km detector [11], we first analyze the PI for the 8 km cavity with RoCs of 3730 m and 4485 m. Other parameters are listed in table 1.

We analyzed the parametric gains for 8140 acoustic modes, of which 3561 modes with $R > 0$, from 3 kHz to 100 kHz interacting with up to 10th order optical modes in 5 free spectral ranges. In figure 1, the dots represent all the parametric gains larger than 10^{-10} of test mass acoustic modes in an 8 km cavity. It can be seen that the highest frequency of unstable mode is around 40 kHz in this analysis. We assume the same Q_{m} for all the acoustic modes. However, previous research showed that Q_{m} is actually frequency dependent [29, 30] for fused silica, with higher order acoustic modes tending to have lower Q_{m}. These give us good reasons to

Table 1. Main parameters of the detectors used in this paper are listed in this table. Values shown outside the brackets indicate the initial values considered in figure 1. Values shown in brackets indicate parameters for which a range of values was considered. Beam sizes on both mirrors are fixed in this paper as discussed in section 4.1.

Parameter	Value
Mirror substrate	Fused silica
Mirror radius	0.25 (0.25–0.26) m
Mirror thickness	0.20 m
Beam radius on ITM/ETM	0.106 m/0.124 m
Mirror mass, M	87 (87–94) kg
Final stage temperature	293.15 K
Acoustic mode quality factor, Q_{m}	10^7
Central RoC of ITM/ETM	3730 m/4485 m
Cavity length, L	8 (6–10) km
Finesse, $\mathcal{F}$	450
Wavelength, λ	1064 nm
Intra-cavity power, P	830 kW
Free spectral range, FSR	18 750 Hz
Mode spacing, $\lvert\omega_{00} - \omega_{01}\rvert$	1954 Hz

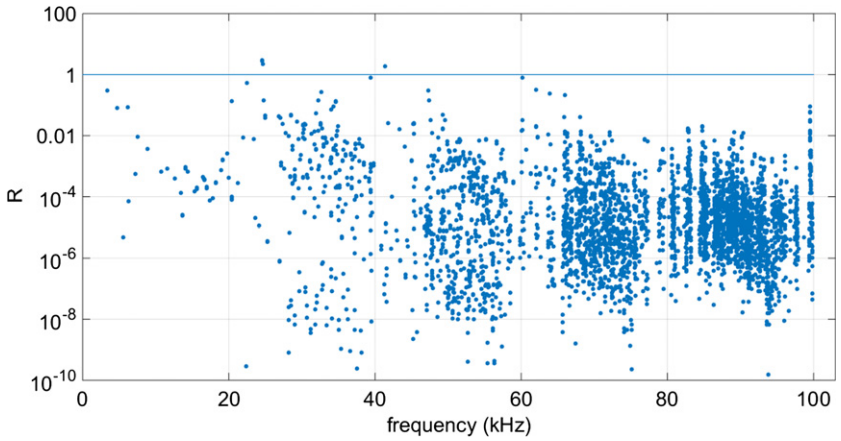

Figure 1. Parametric gain for acoustic modes interacting with optical modes of up to the 10th order. The horizontal axis represents the frequency of the acoustic mode; the vertical axis represents the parametric gain. The horizontal line indicates unity gain. Four unstable modes appear above this line in this particular case.

believe acoustic modes higher than 100 kHz will have no contribution to PI. There are three unstable modes with 830 kW intra-cavity power in the cavity and the largest parametric gain is 2.9. This indicates that the cavity will start to become unstable with intra-cavity power of 287 kW. There are also 27 acoustic modes with $R > 0.1$ and 375 with $R > 10^{-3}$. There would be 14 unstable modes when the power reaches 5 MW. From these statistics the rapid increase in number of instabilities with increasing power can be inferred by scaling the parametric gain by the power ratio of desired power divide by 830 kW.

Note in figure 1 that the gain values align vertically. The phenomenon is more obvious at higher frequencies. This structure arises due to the matching between the frequency of the

acoustic mode with that of optical beating mode according to equation (2). The parametric gain can exceed unity only if the frequency of the acoustic mode is close to the frequency difference between the optical modes. Thus the x-axis values of the vertical lines match with the frequency differences between the higher order modes and the fundamental mode.

In the above analysis, we estimated the diffraction loss using the clipping approximation. This method assumes that the mode shape is not altered by the finite-mirror geometry and that the diffraction loss is simply determined by the fraction of the mode that overlaps the mirror. A general rule of thumb is that when the order of the optical mode is larger than $\left(\frac{\text{mirror diameter}}{\text{beam size}}\right)^2 \approx 5$, clipping loss is negligible. As the beam size gets bigger for higher order optical modes, clipping losses increase with an associated decrease in $Q_{\text{s/a}}$ and reduced parametric gain. This can be seen in figure 1 where the parametric gain is relatively large close to integer multiples of the free spectral range and then reduces as the frequency increases to the next multiple of the free spectral range, where lower order optical modes are again resonant. Besides, the parametric gain is tend to reduce with higher frequency also because that $R \propto \frac{1}{\omega_{\text{m}}^2}$.

4. Optimization of PI-free window

4.1. Altering the radius of curvature

In this section the analysis from section 3 is repeated for a range of test mass radii of curvature. The same parameters are used other than the RoC of end test mass (ETM) which is varied from 4400 m to 4570 m. We note that varying the RoC would introduce the change in beam size and furthermore influence the overlapping factor Λ and the result in section. 4.1. However, in this paper we mainly focus on the acoustic modes that have large parametric gain. These modes tend to have very large Λ that is not susceptible to the beam size change. We analyzed how the largest possible change in RoC would affect the PI-free window, as a result of changes in the Λ. For the 8 km arm cavity, while altering the RoC by the maximum change of 210 m, the beam size changes from 0.124 m to 0.120 m, resulting in maximum R changing from 2.89 to 2.93. Using these two extreme ranges of the beam size in the simulation for all the RoC, results in a PI-free window at the same position as that in figure 2(a) with window size between 6.8 m and 5 m respectively. Considering calculating the overlapping factor Λ is extremely computationally expensive, and the previous analysis show for small changes which does not affect the result much, we did not do the full analysis in this paper. But for a final design for a detector, it is worthwhile to do the full analysis.

The results are presented in figure 2 as the maximum parametric gain and the number of unstable modes at different RoC. The maximum PI gain shows the required control strength, while the number of unstable mode shows the control complexity. Both of them show the difficulty in PI control.

In figure 2(a), each point represents the PI gain of one acoustic mode that is the highest among all the acoustic modes considered at that particular RoC. Data below the unity gain horizontal line indicates that the system is free of PI. Figure 2(b) shows the number of unstable modes for each ETM RoC. We can see that around RoC of 4500 m there is a 6.8 m PI-free window. Figure 2(b) reveals that there is only one unstable mode, which is the peak in figure 2(a) between 4490 m and to 4500 m. Hence if combined with active damping, the PI-free window can be enlarged to 14 m. This analysis could be used for thermal tuning at room temperature or parameter selection for cryogenic operation where thermal tuning is not available.

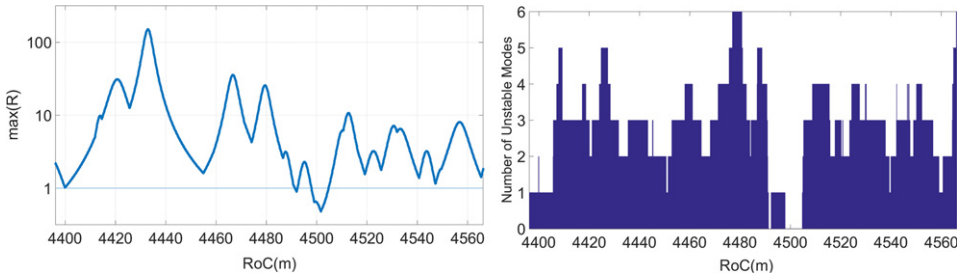

Figure 2. (a) The maximum gain at each RoC, and (b) the number of unstable modes as the RoC is varied. The model uses test mass parameters listed in table 1.

4.2. Altering cavity length

Changing the cavity length is another option at the detector design stage. Generally, the longer the arm length, the longer the light spends interacting with a gravitational wave, resulting in a larger change in phase of the light and improved gravitational wave detector sensitivity. In this section we explore this parameter space by varying the cavity length from 6 km to 10 km while maintaining approximately the same beam size on each test mass.

The beam size is fixed by setting the initial RoC. This condition is chosen because coating thermal noise, which scales inversely to beam size, is a dominant noise source in current detectors. Therefore maintaining beam size in some sense maintains a certain interferometer noise performance. To satisfy the beam size condition, the central RoC of ETM is varied from 3250 m to 4360 m as the cavity length is varied from 6 to 10 km. From this initial condition we vary the RoC from $+40$ m to $+210$ m, this RoC range maintains a stable cavity such that $0 < g_1 g_2 = \left(1 - \frac{L}{\mathrm{RoC}_1}\right)\left(1 - \frac{L}{\mathrm{RoC}_2}\right) < 1$. Figure 3 shows a scan of the maximum parametric gain at different cavity length and RoC.

In figure 3, the maximum parametric gain R is indicated by different colors: dark blue indicates a small parametric gain while bright yellow indicates a large parametric gain. A continuous yellow line indicates that the same unstable acoustic mode will be present over a range of cavity length and RoC. The optimal design, i.e. the largest PI-free window can be found from this figure by locating the largest dark blue vertical RoC range. For this test mass with parameters listed in table 1, we found that the largest PI-free window is at cavity length of 6220 m with a window size of 32.9 m, marked with pink stars at the upper left corner in figure 3, almost five times larger than the window at cavity length of 8 km presented in section 4.1. The maximum R and the number of unstable modes at cavity length of 6220 m is shown in figure 4.

4.3. Altering mirror diameter

For a fixed length detector, an alternate method is to modify the size or material of the test mass to avoid PI. Here we analyze how the size of a test mass affects PI. Larger test masses have higher acoustic mode density, and lower eigen-frequencies. This changes parametric gain by modifying the resonance condition according to equation (2). Heavier test masses in general lower radiation pressure noise—a noise due to quantum amplitude fluctuations in the light driving test mass motion which affects 10–60 Hz in observation run 3 sensitivity. Therefore in general heavier test masses are more desirable in terms of radiation pressure noise. Furthermore, the test mass with larger diameter would also have smaller diffraction loss. In this section we will demonstrate how a desired PI-free window can be obtained at a certain cavity length

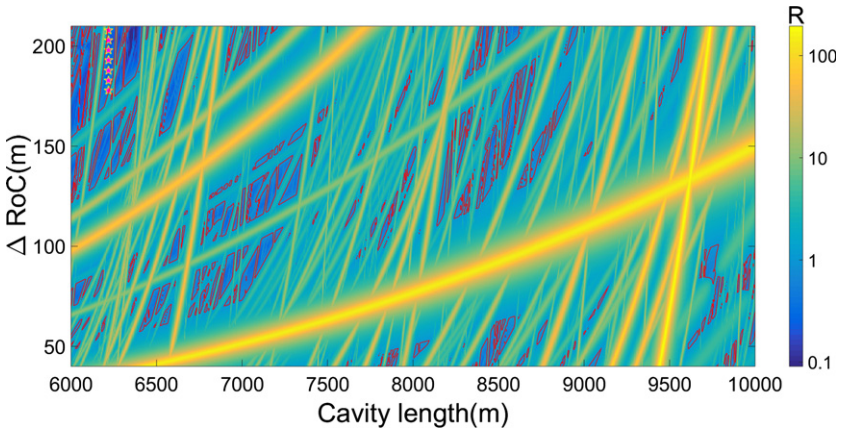

Figure 3. Maximum parametric gain for different cavity lengths from 6 km to 10 km with initial RoC +40–210 m. The PI gain value is represented by the color. Regions with $R < 1$ are marked with a red perimeter. The longest continuous vertical region is marked with pink stars.

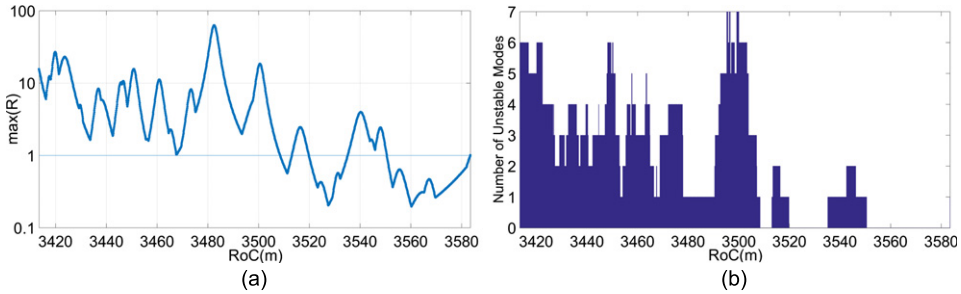

Figure 4. The maximum gain (a) and the number of unstable modes (b) as a function of mirror RoC at cavity length of 6220 m.

by varying test mass dimensions. In our analysis, we consider the case of 8 km length detector with different test mass sizes. There are four test masses with same thickness while diameters change incrementally by 0.5 cm respectively.

Figure 5 shows the maximum parametric gain changes with RoC for five test mass sizes. It can be seen that by increasing the test mass diameter, the peak PI marked with the red arrow, as well as the PI-free window, shifts to a lower RoC. Note that this peak is the result of a particular acoustic mode interacting with the same higher order mode. This is because as the test mass dimension increases, the frequency of the acoustic mode with the same mode shape decreases. Therefore a particular acoustic mode in a larger test mass will interact with the same optical mode at a smaller RoC.

It also can be seen that the PI-free window size changes when the mirror diameter changes. Although there is an approximately proportional relation between acoustic mode frequency and test mass size, and a rough proportionality of the mode spacing change with the RoC within a small range, the rate of change varies for each individual acoustic mode, it is difficult to distinguish the trend from figure 5 alone. The complex parameter set makes it difficult, but still possible to explore analytically for the purpose of finding largest PI-free windows. It should

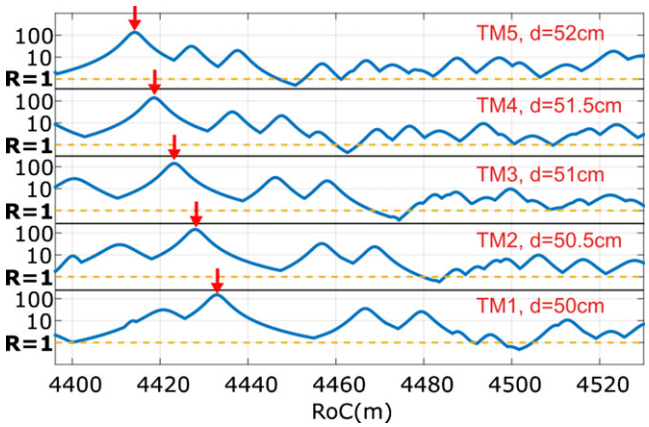

Figure 5. Maximum parametric gain at different RoC for different test masses' diameters for an 8 km cavity. From top to bottom, the diameter of the test mass decreases in steps of 0.5 cm. The dotted lines indicate the PI threshold for each case.

Table 2. Comparison of the sizes of the largest PI-free windows for different test masses at 8 km and around 6200 m cavity length.

	TM 1	TM 2	TM 3	TM 4	TM 5
Diameter (cm)	50.0	50.5	51.0	51.5	52.0
PI-free window at 8 km (m)	6.8	5.1	8.4	5.1	5.8
PI-free window at L_{opt} (m)	32.9	38.5	42	43.3	45.1
Optimal cavity length, L_{opt} (m)	6220	6210	6215	6215	6335

be possible that the full parameter space can be mapped and trends identified with sufficient simulation time.

4.4. Optimization of the test mass diameter and cavity length

Table 2 compares the largest PI-free window size at 8 km and the largest PI-free window in figure 3 around cavity length of 6200 m, with 5 different test mass sizes.

It is important to consider the PI-free window results in relation to the dynamics in a real interferometer cavity. In these cavities, the optical absorption heating of the test mass would modify the RoC of test mass and deform the test mass through thermal expansion. These variations would modify the cavity mode matching and cause transient PI [31] after initial cavity locking. Considering a cavity with intra-cavity power of 830 kW and 0.5 ppm coating absorption for ETM only, the change of the RoC due to optical absorption is about 34.7 m [32]. From table 2, it can be seen that in an 8 km cavity, the PI-free window with any of the 5 test mass sizes is not big enough to maintain stability. However, the largest PI-free window with 6335 m cavity length and 52 cm test mass is 45.1 m which is larger than the variation expected from laser power effects. Combined with appropriate thermal compensation to keep the change of RoC in a small range, the PI-free interferometer could be realized. Even in cryogenic situation where thermal compensation is not available, a PI-free window design approach will still be effective. Unfortunately, for circulating power up to 3 MW, none of the PI-free window considered in this paper is sufficient to compensate the RoC change due to the coating absorption.

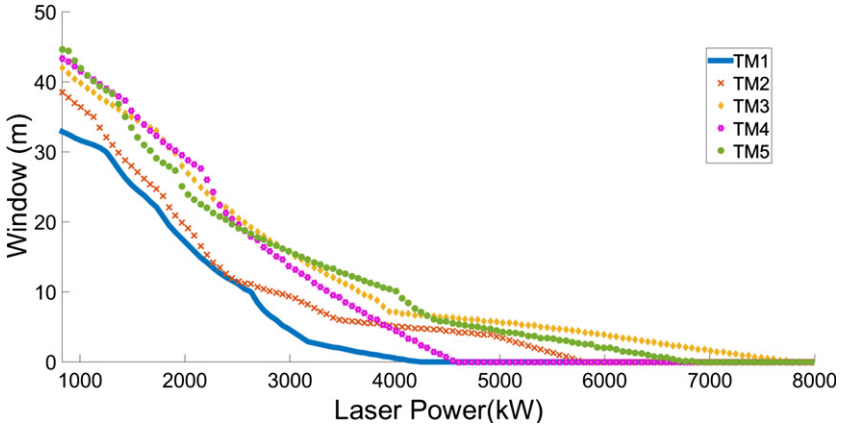

Figure 6. The size of the largest window for each test mass verses laser power.

4.5. PI-free window size in high intra-cavity power

The above simulation uses the aLIGO designed intra-cavity power of 830 kW [33]. Since PI is proportional to intra-cavity power in the arm cavity, the size of PI-free window shrinks proportionally at higher power. In figure 6, we show how the PI-free window size decreases with increased power for each of the optimized design listed in table 2. It can be seen that the PI-free window size decreases at about the same rate for all test masses considered. There is a change in slop at around 4500 kW. It can be seen that within the largest PI-free window shown in figure 4(a), as the power goes higher, some new modes would be unstable and the window can be broken into several smaller PI-free windows. The remaining largest PI-free window now is bounded by different acoustic modes. If the parametric gain of the new unstable mode changes in different rate as RoC, the slop in figure 6 would change. At intra-cavity power of 5 MW, the case with larger test masses will have PI-free windows of several meters. None of the cases in our simulation will have a PI-free window with 8 MW intra-cavity power. Besides, the thermal expansion effect would be more significant when the power goes higher. Multiple methods should be applied simultaneously to solve PI in such case.

5. Uncertainty analysis

It is impossible to know the precise value for every parameter that affects parametric gain in real interferometers. Unavoidable imperfection in mirror fabrication, temperature change caused by laser heating and the precision of finite element modeling will limit the accuracy in acoustic mode displacement field and resonant frequency [34]. Errors in cavity length and RoC will also affect the resonance condition. A constant $Q_{\mathrm{m}} = 10^7$ for all the acoustic modes is assumed in our analysis, which is representative of measured Q's of LIGO test masses. Some measured Q's are a factor of a few larger, while for many higher frequency mode Q's a much smaller. In our simulation, we scanned the mode orientation to achieve the largest overlapping factor and assumed the alignment is perfectly centered. Experimental result shows that the overlapping factor is very sensitive to the alignment and the rotation angle between acoustic and optical modes [35].

Statistic result shows that the error in cavity resonance condition defined in equation (8) has the biggest impact on the results. In general, the error arises from the resonance condition can

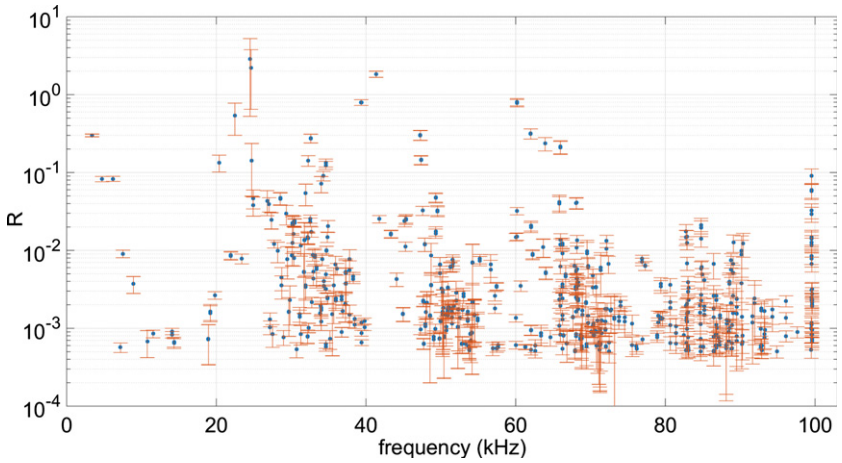

Figure 7. The uncertainty of parametric gain larger than 10^{-3} in figure 1.

be expressed as the sum of the uncertainties of Stokes and anti-Stokes gain [36]:

$$(\sigma_R)^2 = \left(\sigma_{R_\mathrm{s}}\right)^2 + \left(\sigma_{R_\mathrm{a}}\right)^2, \tag{4}$$

where

$$\left(\sigma_{R_\mathrm{s}}\right)^2 = \left(\frac{\partial R_\mathrm{s}}{\partial \Delta\omega_\mathrm{s}}\right)^2 \left(\sigma_{\Delta\omega_\mathrm{s}}\right)^2 + \left(\frac{\partial R_\mathrm{s}}{\partial \omega_\mathrm{m}}\right)^2 \left(\sigma_{\omega_\mathrm{m}}\right)^2 + 2\frac{\partial R_\mathrm{s}}{\partial \Delta\omega_\mathrm{s}}\frac{\partial R_\mathrm{s}}{\partial \omega_\mathrm{m}}\,\mathrm{cov}\left(\Delta\omega_\mathrm{s}, \omega_\mathrm{m}\right), \tag{5}$$

and

$$\frac{\partial R_\mathrm{s}}{\partial \Delta\omega_\mathrm{s}} = -\frac{2R_\mathrm{s}\Delta\omega_\mathrm{s}}{\delta^2 + (\Delta\omega_\mathrm{s})^2} \tag{6}$$

$$\frac{\partial R_\mathrm{s}}{\partial \omega_\mathrm{m}} = -\frac{2R_\mathrm{s}}{\omega_\mathrm{m}}, \quad \mathrm{cov}\left(\Delta\omega_\mathrm{s}, \omega_\mathrm{m}\right) = -\sigma_{\omega_\mathrm{m}}, \tag{7}$$

$$\left(\sigma_{\Delta\omega_\mathrm{s}}\right)^2 = \left(\frac{\partial \Delta\omega_\mathrm{s}}{\partial \mathrm{RoC}_1}\sigma_{\mathrm{RoC}_1}\right)^2 + \left(\frac{\partial \Delta\omega_\mathrm{s}}{\partial \mathrm{RoC}_2}\sigma_{\mathrm{RoC}_2}\right)^2 + \left(\frac{\partial \Delta\omega_\mathrm{s}}{\partial L}\sigma_L\right)^2 + \left(\sigma_{\omega_\mathrm{m}}\right)^2 \tag{8}$$

Here we assume that $\sigma_{\mathrm{RoC}_{1,2}} \approx 0.5\%\,\mathrm{RoC}_{1,2}$, cavity length is 8000 m $\pm$ 2 mm. With very fine mesh used in FEM to determine the resonance of the acoustic mode, we consider $\sigma_{\omega_\mathrm{m}} = 0.1\%\,\omega_\mathrm{m}$ for ω_m up to 100 kHz. An estimation on uncertainty is shown in figure 7. We used same parameters to calculate parametric gain as those in figure 1. Only the modes with $R > 0.001$ are shown here. Besides, R is proportional to Q_m, Q_s, Λ and P. The uncertainty in R should be sum of all these uncertainties plus the uncertainty due to the resonance condition. The Q_m is an assumed value. Any difference in Q_m will directly affect the R value. We have estimated the largest uncertainty in Λ is 1.7% in section 4.2. The eigenfrequency change resulting from temperature is not considered. However, the expected maximum change is about 10 Hz, it is insignificant relative to the changes in optical mode frequency.

The PI free window depends on all potential unstable acoustic modes within the window. The PI gain of each mode depends dominantly on the resonant condition, and is a Lorentz

function of the frequency mismatch, $\Delta\omega_s$. The error in PI free window size comes from the error in estimation of the individual acoustic mode frequency and corresponding optical cavity mode frequencies. The dominate ones are the optical cavity mode spacing error induced by the test mass radii of curvature error in manufacturing and the acoustic mode frequency error in FEM simulation. Considering the highest frequency of the unstable mode is 40 kHz with 0.1% uncertainty in acoustic mode frequency and a 45.1 m PI-free window, the error in frequency mismatch $\Delta\omega_s$ would be 10%, which is the worst case in estimation error of the PI free window. We note that altering RoC would change the beam spot size on both mirrors which is not considered in this paper. It would affect the accuracy in analyzing overlapping factor and diffraction loss, and hence the PI free window size, but less than the resonance condition.

6. Conclusion

In this paper we investigated parametric instability for a range of lengths of simple optical cavities from 6–10 km. The main focus of this paper was to explore whether the PI could be avoided by carefully choosing certain parameters of the interferometer. Based on a single cavity simulation, we found that it is possible to have PI-free windows for a reasonable range, up to 45 m, of RoC change in the long cavities studied, allowing for manufacturing tolerances and thermal distortions in the mirrors at 830 kW intra-cavity power. For higher intra-cavity power, the PI-free windows shrink accordingly. At some power level, there would not be any PI-free window, and PI cannot be avoided by design. However even in such situation, the procedures presented here will still assist to find some PI-low windows, thereby reducing the demands of acoustic mode dampers or other methods of suppression PI.

The simple cavity model we used here would give an indication of the trend for designing PI-free detectors. For full interferometer designs, it will be necessary to consider more realistic situations including the recycling cavities, the Gouy phases of higher order modes, and details of test masses such as flats and bevels, as well as AMDs on the test masses, to ensure that PI-free windows are optimized as close to real situation as possible.

Acknowledgments

This work is supported by Australian Research Council Discovery Project DP160102447, and Center of Excellence for Gravitational Wave Discovery project CE170100004. Special thanks to Vladimir Bossilkov, Slawomir Gras, Joris van Heijningen and Carl Blair for valuable discussions and suggestions.

ORCID iDs

Jue Zhang https://orcid.org/0000-0002-3931-3851

References

[1] Aasi J, Abbott B P, Abbott R, Abbott T, Abernathy M R, Ackley K, Adams C, Adams T, Addesso P, Adhikari R X *et al* 2015 Advanced LIGO *Class. Quantum Grav.* **32** 074001

[2] Acernese F, Agathos M, Agatsuma K, Aisa D, Allemandou N, Allocca A, Amarni J, Astone P, Balestri G, Ballardin G *et al* 2014 Advanced Virgo: a second-generation interferometric gravitational wave detector *Class. Quantum Grav.* **32** 024001

[3] Abbott B P *et al* 2019 LIGO Scientific GWTC-1: a gravitational-wave transient catalog of compact binary mergers observed by LIGO and Virgo during the first and second observing runs *Phys. Rev. X* **9** 031040
[4] Abbott B P, Abbott R, Abbott T D, Acernese F, Ackley K, Adams C, Adams T, Addesso P, Adhikari R X, Adya V B *et al* 2017 GW170817: observation of gravitational waves from a binary neutron star inspiral *Phys. Rev. Lett.* **119** 161101
[5] O3 Events Public 2019 GraceDB — Gravitational-Wave Candidate Event Database https://gracedb.ligo.org/superevents/public/O3/
[6] Chirps 2019 Chirp - Keep track of the latest gravitational wave alerts http://chirp.sr.bham.ac.uk/alerts
[7] Aso Y, Michimura Y, Somiya K, Ando M, Miyakawa O, Sekiguchi T, Tatsumi D, Yamamoto H *et al* KAGRA Collaboration 2013 Interferometer design of the KAGRA gravitational wave detector *Phys. Rev. D* **88** 043007
[8] Unnikrishnan C S 2013 IndIGO and LIGO-India: scope and plans for gravitational wave research and precision metrology in India *Int. J. Mod. Phys. D* **22** 1341010
[9] Punturo M, Abernathy M, Acernese F, Allen B, Andersson N, Arun K, Barone F, Barr B, Barsuglia M, Beker M *et al* 2010 The Einstein telescope: a third-generation gravitational wave observatory *Class. Quantum Grav.* **27** 194002
[10] Abbott B P 2017 *Class. Quantum Grav.* **34** 044001
[11] Blair D, Ju L, Zhao C, Wen L, Miao H, Cai R, Gao J, Lin X, Dong L, Wu L-A *et al* 2015 The next detectors for gravitational wave astronomy *Sci. China Phys. Mech. Astron.* **58** 1–34
[12] Eichholz J 2019 *OzGrav HF Preliminary Design Study* (*LIGO-G1900252*) https://dcc.ligo.org/LIGO-G1900252
[13] Braginsky V B, Strigin S E and Vyatchanin S P 2001 Parametric oscillatory instability in fabry–perot interferometer *Phys. Lett. A* **287** 331–38
[14] Zhao C, Ju L, Qi F, Blair C, Qin J, Blair D, Jerome D and Yamamoto H 2015 Parametric instability in long optical cavities and suppression by dynamic transverse mode frequency modulation *Phys. Rev. D* **91** 092001
[15] Chen X, Zhao C, Danilishin S, Ju L, Blair D, Wang H, Vyatchanin S P, Molinelli C, Kuhn A, Gras S *et al* 2015 Observation of three-mode parametric instability *Phys. Rev. A* **91** 033832
[16] Evans M *et al* 2015 Observation of parametric instability in Advanced LIGO *Phys. Rev. Lett.* **114** 161102
[17] Zhao C, Ju L, Degallaix J, Gras S and Blair D G 2005 Parametric instabilities and their control in advanced interferometer gravitational-wave detectors *Phys. Rev. Lett.* **94** 121102
[18] Blair C, Gras S, Abbott R, Aston S, Joseph B, Blair D, Ryan D, Evans M, Frolov V, Fritschel P *et al* 2017 First demonstration of electrostatic damping of parametric instability at Advanced LIGO *Phys. Rev. Lett.* **118** 151102
[19] Gras S, Fritschel P, Barsotti L and Evans M 2015 Resonant dampers for parametric instabilities in gravitational wave detectors *Phys. Rev. D* **92** 082001
[20] Fan Y, Merrill L, Zhao C, Ju L, Blair D, Slagmolen B, Hosken D, Brooks A, Veitch P and Munch J 2010 Testing the suppression of opto-acoustic parametric interactions using optical feedback control *Class. Quantum Grav.* **27** 084028
[21] Zhang Z, Zhao C, Ju L and Blair D G 2010 Enhancement and suppression of opto-acoustic parametric interactions using optical feedback *Phys. Rev. A* **81** 013822
[22] Rana A *et al* 2015 *LIGO Voyager Upgrade Conceptual Design* https://dcc.ligo.org/LIGO-T1400226
[23] Zhang J, Zhao C, Ju L and Blair D 2017 Study of parametric instability in gravitational wave detectors with silicon test masses *Class. Quantum Grav.* **34** 055006
[24] Gras S, Zhao C, Blair D G and Ju L 2010 Parametric instabilities in advanced gravitational wave detectors *Class. Quantum Grav.* **27** 205019
[25] Green A C, Brown D D, Dovale-Álvarez M, Collins C, Miao H, Mow-Lowry C M and Freise A 2017 The influence of dual-recycling on parametric instabilities at advanced ligo *Class. Quantum Grav.* **34** 205004
[26] Evans M, Barsotti L and Fritschel P 2010 A general approach to optomechanical parametric instabilities *Phys. Lett. A* **374** 665–71
[27] Braginsky V B, Strigin S E and Vyatchanin S P 2002 Analysis of parametric oscillatory instability in power recycled LIGO interferometer *Phys. Lett. A* **305** 111–24
[28] Kogelnik H and Li T 1966 Laser beams and resonators *Appl. Opt.* **5** 1550–567

[29] Numata K, Yamamoto K, Ishimoto H, Otsuka S, Kawabe K, Ando M and Tsubono K 2004 Systematic measurement of the intrinsic losses in various kinds of bulk fused silica *Phys. Lett. A* **327** 263–71
[30] Penn S D, Alexander A, Busby D, Harry G M, Gretarsson A M, Numata K and Willems P 2006 Frequency and surface dependence of the mechanical loss in fused silica *Phys. Lett. A* **352** 3–6
[31] Hamedan V J, Zhao C, Ju L, Blair C and Blair D G 2018 Suppression of thermal transients in advanced LIGO interferometers using CO_2 laser preheating *Class. Quantum Grav.* **35** 115006
[32] Winkler W, Danzmann K, Albrecht R and Schilling R 1991 Heating by optical absorption and the performance of interferometric gravitational-wave detectors *Phys. Rev. A* **44** 7022
[33] Shoemaker D 2001 Advanced LIGO 2002–2006 Presentation at the Aspen Winter Conf. on Gravitational Wave Detection vol 200 https://dcc.ligo.org/LIGO-G010020/public
[34] Strigin S E, Blair D G, Gras S and Vyatchanin S P 2008 Numerical calculations of elastic modes frequencies for parametric oscillatory instability in Advanced LIGO interferometer *Phys. Lett. A* **372** 5727–731
[35] alog 10 kHz P I 2019 aLIGO LHO Logbook https://alog.ligo-wa.caltech.edu/aLOG/index.php?callRep=49747
[36] Gras S, Blair D G and Zhao C 2009 Suppression of parametric instabilities in future gravitational wave detectors using damping rings *Class. Quantum Grav.* **26** 135012